Acta Materialia 241 (2022) 118395

Contents lists available at ScienceDirect

Acta Materialia

journal homepage: www.elsevier.com/locate/actamat

Hetero-zone boundary affected region: A primary microstructural factor controlling extra work hardening in heterostructure

Yanfei Wang[a], Yuntian Zhu[b,*], Zhijie Yu[a], Jianfeng Zhao[c], Yueguang Wei[a,*]

[a] Department of Mechanics and Engineering Science, College of Engineering, Peking University, Beijing 100871, China
[b] Department of Materials Science and Engineering; Mechanical Behavior Division of Shenyang National Laboratory for Materials Science, City University of Hong Kong, Hong Kong, China
[c] Institute of Systems Engineering, Chinese Academy of Engineering Physics, Mianyang 621999, China

ARTICLE INFO

Article history:
Received 3 June 2022
Revised 4 September 2022
Accepted 27 September 2022
Available online 29 September 2022

Keywords:
Heterostructure
Hetero-zone boundary affected region (Hbar)
Strength and ductility
Hetero-deformation induced hardening
Back stress

ABSTRACT

Heterostructured metals possess superior mechanical properties exceeding the prediction by the rule-of-mixtures. However, it remains a challenge to understand the key microstructural factor that controls the extra work hardening. Here aided by a newly developed mechanism-based plasticity model that incorporates the constitutive law of the back stress induced by zone-scale deformation heterogeneity, we reveal that the hetero-zone boundary affected region (Hbar) plays the key role in controlling the synergistic mechanical responses of heterostructure. Specifically, the Hbar, characterized by high strain gradient with a constant characteristic width, is formed to coordinate inter-zone deformation heterogeneity. The extra work hardening originates primarily in the Hbar, where the accumulation of geometrically necessary dislocations develops back stress and forest hardening. Importantly, the extra work hardening increases proportionally with Hbar volume fraction, and the best strength-ductility combination is reached when Hbar approaches saturation. In addition, the influences of zone configuration, mechanical incompatibility, and zone volume fraction on Hbar effect are analyzed, which sheds light on potential strategies to enhance the Hbar effect for optimizing strength-ductility combination.

1. Introduction

For structural applications, metallic materials is expected to be strong and ductile, but these two properties are rarely attainable at the same time [1]. For instance, increasing the density of defects can improve strength, but this is usually accompanied by compromising strain hardening and consequently the uniform elongation (ductility) [2]. Inspired by heterostructures in natural biological systems, extensive attentions have recently been paid to designing metals with heterogeneous microstructure that consists of zones having dramatically different mechanical properties [3,4]. Superior strength-ductility combinations have indeed been achieved in many heterostructured materials [5–21].

The strain hardening and strength of heterostructured materials typically exceed the predictions by the rule-of-mixtures [10,13,22–24]. For instance, the heterogeneous lamella Ti was reported to be as strong as nanostructured (NS) Ti [6], with the strain hardening even much higher than that of its homogeneous coarse-grained (CG) counterpart (Fig. 1A). In a partially recrystallized Cu with ~75% NS [5], the strain hardening was found comparable to that of fully recrystallized CG Cu (Fig. 1B). These exceptional properties suggest that synergistic interaction between heterostructured zones may be activated to generate extra mechanical responses, which is also referred to as synergistic mechanical effects [4,25]. This raises several issues: Where in the heterostructure is the extra work hardening originated? What is the key microstructural factor that determines the development of extra strain hardening? How can the extra work hardening be evaluated based on microstructure heterogeneity? These issues are not only critical to understanding the deformation physics, but also needed for optimizing heterostructure design.

The hetero-zone boundaries are believed to affect the micromechanics and consequently the macroscopic mechanical behaviors [3]. The deformation heterogeneity across zone boundaries causes inter-zone constraint, which changes surrounding stress state and dislocation behavior [13,15,26]. Meanwhile, plastic strain gradient and geometrically necessary dislocation (GND) accumulation inevitably occur near the hetero-zone boundary, which produces long-range internal stress and forest hardening [6,13,14,27].

* Corresponding authors.
E-mail addresses: y.zhu@cityu.edu.hk (Y. Zhu), weiyg@pku.edu.cn (Y. Wei).

https://doi.org/10.1016/j.actamat.2022.118395

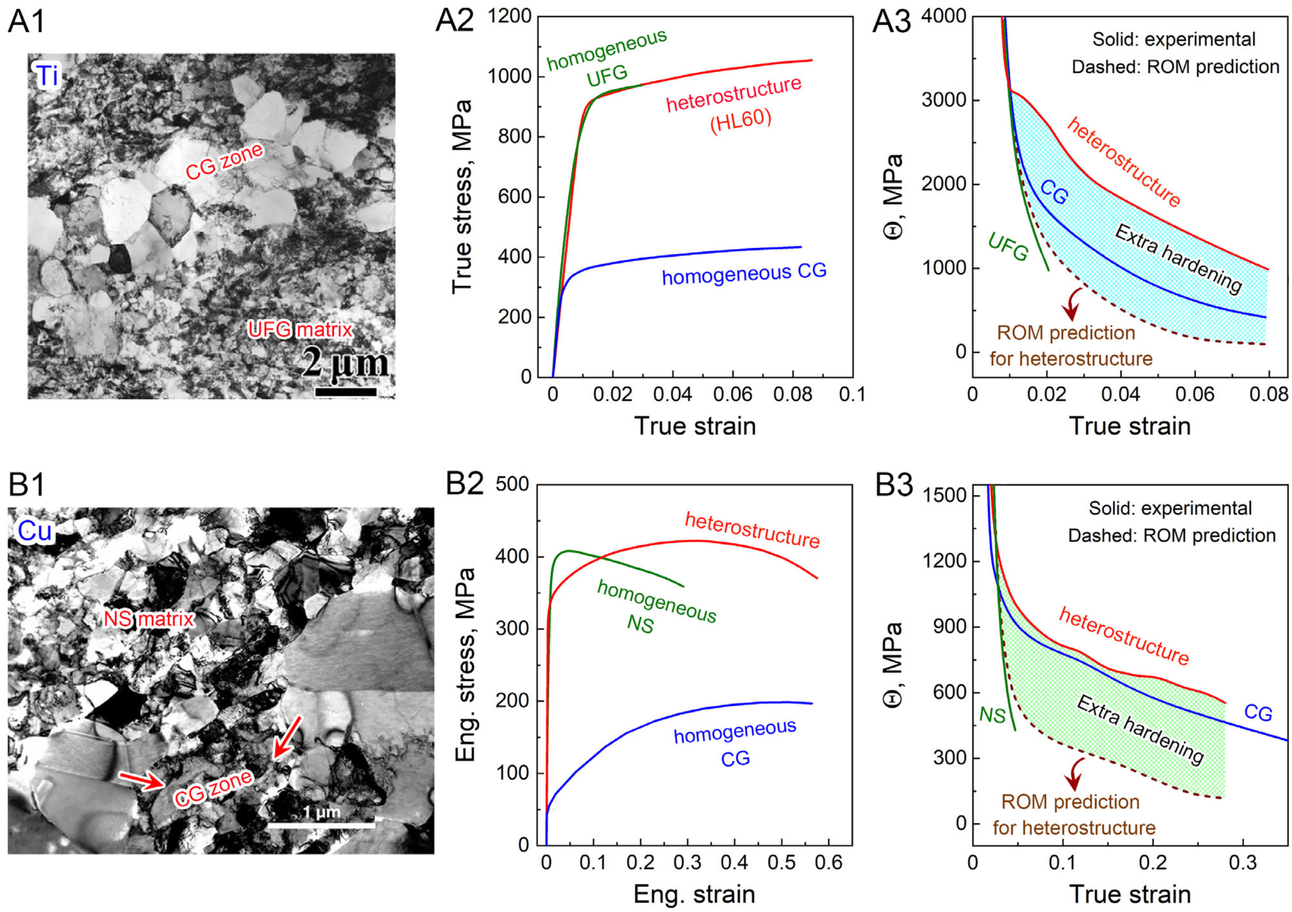

Fig. 1. Synergistic work hardening in (A1–A3) heterostructured lamellar Ti [6] and (B1–B3) heterostructured Cu [5]. Strain hardening rate (Θ) evolutions are plotted in (A3) and (B3), in which the dashed lines represent the predictions by rule-of-mixtures (ROM) based on the responses of their freestanding homogeneous counterparts. The shadow regions indicate the synergistic strain hardening.

However, it remains a grand challenge to quantitatively evaluate hetero-zone boundary effect, especially on the extra work hardening. In the gradient heterostructure, extra hardening peak, which moves with migrating interface between plastically unstable NS surface and stable CG core, was detected by micro-hardness testing [13]. But for the sharp NS/CG boundary, the limited span of hetero-zone boundary affected region cannot be effectively resolved by general mechanical means [14]. On the other hand, synergistic mechanical responses may also be affected by the configuration, volume fraction and intrinsic properties of constituent zones, since they are potential factors affecting either the intensity or spatial density of inter-zone interaction [23,28–30]. Despite previous efforts, it remains challenging to understand the aforementioned issues. The limitations of experimental exploration lie in the limited characterization capability for zone boundary micromechanics and the convoluted effects of numerous microstructural factors.

Physics-based constitutive modeling is an efficient way to analyze the mechanical effect of designated mechanism and/or microstructural factor. Using finite element methods (FEM), the deformation heterogeneity-induced inter-zone constraint can be taken into account [30]. Indeed, various constitutive models have been proposed to describe the strength, strain hardening and sometimes also failure behavior of the bimodal heterostructure [31,32], gradient heterostructure [33–36], harmonic heterostructure, etc. [37,38]. However, effects of the hetero-zone boundary and the zone-scale strain heterogeneity were always ignored, and the GND effect considered was only that intrinsic to grains [31,34]. Recently, after experimentally confirming the strong deformation heterogeneity, Li et al. established additional back stress term in the dislocation density-based models, by injecting GNDs to coordinate the inter-zone strain difference [39–42]. To address the effect of hetero-zone boundary in CG/NS laminates, Zhao et al. mechanically partitioned the affected region, and then implanted an enhanced GND multiplication law in a framework that is the same to that of intragranular GNDs [43]. While the synergistic mechanical responses can be described to some extent by these new models, the zone-scale strain heterogeneity-related constitutive terms depended largely on the particular strain configuration of specific heterostructure. Therefore, a concise-yet-universal constitutive law for the zone-scale deformation heterogeneity is needed.

In this work, we have explored the aforementioned issues through constitutive modeling. Since heterostructures share unifying deformation fundamentals in inter-zone interaction [4], a NS/CG heterostructure in Cu with tunable microstructure is taken as a model heterostructure. In Section 2, a mechanism-based plasticity model incorporating the constitutive law of zone-scale strain heterogeneity is established, which ends with deliberate parameterization and validation. In Section 3, the effects of the commonly tunable microstructural factors, including the zone configuration, mechanical incompatibility and zone fraction, on the macroscopic mechanical response and micromechanics are simulated and analyzed, in order to find the unified key microstructure factor that controls synergistic work hardening. Section 4 discusses the relationship between the key microstructural factor and synergistic mechanical responses. Finally, reasonable answers for the issues are addressed in Section 5.

2. A mechanism-based plasticity model

In constitutive modeling, heterostructures can generally be considered as composites for simplification [40,43]. With the use of FEM, the inter-zone interaction and the strain heterogeneity across hetero-zone boundaries can naturally be generated. Since the grain size-dependent behavior of a freestanding homogeneous zone has been well described in conventional theories, such as the widely used dislocation density-based models [34,44–47], the theoretical key for a zone in heterostructure is incorporating the constitutive law of additional zone-scale deformation heterogeneity [40–42]. Here, the constitutive model for zones in heterostructure is developed based on the framework of conventional mechanism-based strain gradient plasticity (CMSG) proposed by Huang et al. [48], and zone-scale 3D plastic strain gradient is considered in terms of the back stress and forest hardening effects of GNDs accumulation.

2.1. Constitutive framework for the constituent zone in heterostructure

For an elastoplastic constituent zone, the strain rate $\dot{\varepsilon}_{ij}$ can be decomposed into elastic and plastic parts

$$\dot{\varepsilon}_{ij} = \dot{\varepsilon}^e_{ij} + \dot{\varepsilon}^p_{ij}. \tag{1}$$

The elastic part $\dot{\varepsilon}^e_{ij}$ can be expressed by the stress rate $\dot{\sigma}_{ij}$ via Hooke's law

$$\dot{\varepsilon}^e_{ij} = \frac{1}{2\mu}\dot{\sigma}'_{ij} + \frac{\dot{\sigma}_{kk}}{9K}\delta_{ij}, \tag{2}$$

where μ and K are shear and bulk moduli, respectively. $\dot{\sigma}'_{ij} = \dot{\sigma}_{ij} - \frac{1}{3}\dot{\sigma}_{kk}\delta_{ij}$ is the deviatoric stress rate. Based on the J_2-flow theory of plasticity, the plastic strain rate $\dot{\varepsilon}^p_{ij}$ is proportional to the deviatoric stress σ'_{ij},

$$\dot{\varepsilon}^p_{ij} = \frac{3\dot{\varepsilon}^p}{2\sigma_e}\sigma'_{ij}, \tag{3}$$

where $\sigma'_{ij} = \sigma_{ij} - \frac{1}{3}\sigma_{kk}\delta_{ij}$, and $\sigma_e = \sqrt{\frac{3}{2}\sigma'_{ij}\sigma'_{ij}}$ is the von Mises effective stress. $\dot{\varepsilon}^p = \sqrt{\frac{3}{2}\dot{\varepsilon}^p_{ij}\dot{\varepsilon}^p_{ij}}$ is the equivalent plastic strain rate. Following the CMSG plasticity [48], a viscoplastic-like kinetic expression is employed to provides $\dot{\varepsilon}^p$ in terms of σ_e

$$\dot{\varepsilon}^p = \dot{\varepsilon}\left(\frac{\sigma_e}{\sigma_f}\right)^m, \tag{4}$$

where $\dot{\varepsilon} = \sqrt{2\dot{\varepsilon}'_{ij}\dot{\varepsilon}'_{ij}/3}$ is the effective strain rate, and $\dot{\varepsilon}'_{ij} = \dot{\varepsilon}_{ij} - \dot{\varepsilon}_{kk}\delta_{ij}/3$. The rate sensitivity exponent m generally takes a large value. The flow stress σ_f controls the plastic flow, which is determined by the microstructure characteristics and deformation mechanism, as analyzed below.

2.2. Deformation mechanism-based flow stress

For the constituent zones in a heterostructure, the inter-zone constraint rendered by the deformation incompatibility is capable of producing gradient strain distribution (Fig. 2A and B). The zone-scale plastic strain gradient needs to be accommodated by the polarized distribution of GNDs (Fig. 2C), which leads to extra strengthening [27,49]. First, similar to statistically stored dislocations (SSDs), GNDs contribute to isotropic hardening [50,51], from which the contribution on flow stress is referred to as $\sigma_{Taylor,GND}$. Second, the polarized distribution of GNDs produces zone-scale long-range internal stress (Fig. 2D), which is opposite to the applied stress, i.e., zone-scale back stress $\boldsymbol{\sigma}_b$, contributing to kinematic hardening [6,39,52,53]. Third, the GNDs interact with mobile dislocations to further promote the accumulation of SSDs [51]. Given the focus on monotonic uniaxial tension, the zone-scale back stress can be equivalently represented as an isotropic term. Therefore, the first two effects can be directly incorporated into the flow stress as

$$\sigma_f = \sigma_0 + \sigma_{GB} + M\alpha\mu b\sqrt{\rho_{SSD} + \rho_{GND}} + \sigma_b. \tag{5}$$

σ_0 is the lattice friction stress. $\sigma_{GB} = k_{HP}/\sqrt{d}$ represents the grain boundary strengthening, where k_{HP} is the Hall-Petch slop and d is grain size. $M\alpha\mu b\sqrt{\rho_{SSD} + \rho_{GND}}$ is the Taylor flow stress term, where M, α, b, ρ_{SSD} and ρ_{GND} are the Taylor factor, the Taylor constant, the magnitude of Burgers vector, the density of SSDs and GNDs, respectively.

The evolution of ρ_{SSD} with respect to the equivalent plastic strain ε^p can be expressed by the modified Kocks-Mecking-Estrin model [34,42–47]

$$\frac{\partial\rho_{SSD}}{\partial\varepsilon^p} = M\left(\frac{k_1}{bd} + \frac{k_2}{b}\sqrt{\rho_{SSD} + \rho_{GND}} - k_3\left(\frac{\dot{\varepsilon}^p}{\dot{\varepsilon}_0}\right)^{-\frac{1}{n_0}}\rho_{SSD} - \left(\frac{d_{ref}}{d}\right)^2\rho_{SSD}\right). \tag{6}$$

On the right side, the 1st term considers the grain boundary-enhanced dislocation storage, where k_1 is a geometric factor. The 2nd term describes the free slip path-dependent dislocation multiplication, which incorporates the third effect of GNDs. k_2 is a proportionality factor. The 3rd term considers the dynamic recovery, which is approximately considered to be independent of GNDs [40,42]. k_3, $\dot{\varepsilon}_0$ and n_0 are recovery factor, reference strain rate and dynamic recovery exponent. The last term describes the additional annihilation effect due to grain boundary, where d_{ref} is the reference grain size [34,39]. As grain size decreases to certain extent, the d-dependent first and last terms will dominate the accumulation and density limit of SSDs. But effects of the middle two terms will gradually become prominent with increasing grain size.

At the zone scale, GNDs may distribute across several grains. The density was derived as proportional to the effective plastic strain gradient η^p [50,54],

$$\rho_{GND} = \bar{r}\frac{\eta^p}{b}, \tag{7}$$

where $\bar{r}$ is the Nye factor [55]. η^p was derived as $\eta^p = \sqrt{\frac{1}{4}\eta^p_{ijk}\eta^p_{ijk}}$, and $\eta^p_{ijk} = \varepsilon^p_{ik,j} + \varepsilon^p_{jk,i} - \varepsilon^p_{ij,k}$. It has been confirmed in *in-situ* TEM observation that GND piling-up against a hetero-zone boundary cannot increase continuously with strain gradient, which will reach dynamic saturation at a density threshold [56,57]. In the FEM simulation, therefore, a saturation of GNDs density, ρ^{max}_{GND}, is needed [38,58]. Reaching ρ^{max}_{GND} generally implies that the local region loses capability for further work hardening.

2.3. Zone-scale back stress

It is the gradient of GNDs field contributed to the net long-range internal stress. Here, for simplification, all GNDs are assumed to be edge type. Taking a position at the origin of a local coordinate system, such as at a Gaussian integration point in FEM route, the GNDs field can be approximated by a first-order expansion

$$\rho_{GND} = \rho^0_{GND} + \frac{\partial\rho_{GND}}{\partial x}x + \frac{\partial\rho_{GND}}{\partial y}y + \frac{\partial\rho_{GND}}{\partial z}z. \tag{8}$$

It is assumed that the plastic strain gradient along x_i, i.e., $\frac{\partial\eta^p}{\partial x_i}x_i$, is fully accommodated by a set of dislocations in the orientation of $\boldsymbol{b}\|x_i$,and this set of dislocations has no heterogeneity in other directions. This implies that the GND gradient along x_i, i.e., $\frac{\partial\rho_{GND}}{\partial x_i}x_i$, is constituted by a set of $\boldsymbol{b}\|x_i$ oriented dislocations. This strain gradient-GNDs scenarios can be exemplarily rationalized in a 1D

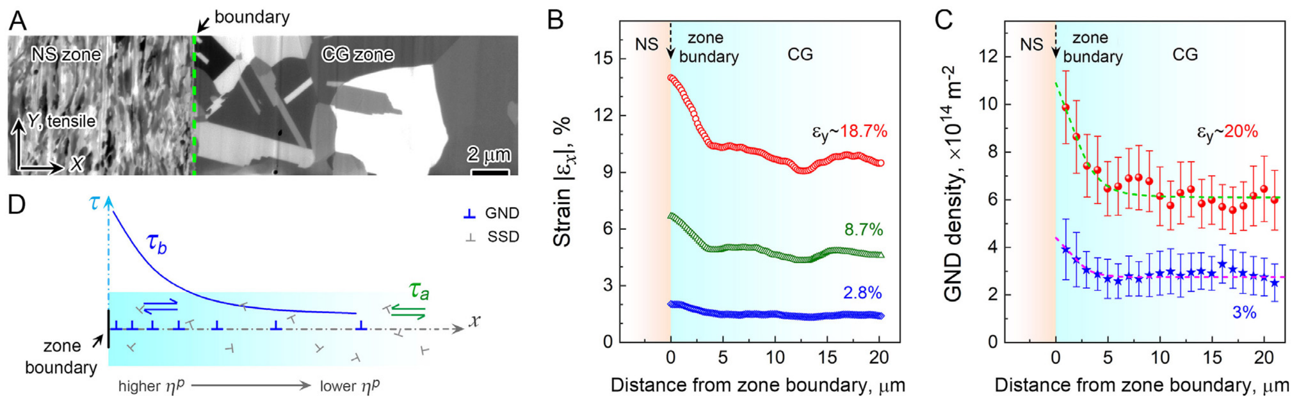

Fig. 2. (A) Representative NS/CG hetero-zone boundary in heterostructures. Gradient distribution of (B) strain and (C) GND density near hetero-zone boundary, after certain tensile strain ε_y [14,15]. (D) A schematic illustration of GND piling-up near a hetero-zone boundary and the long-range back stress τ_b arising therefrom. τ_a indicates resolved external stress.

case like the scheme shown in Fig. 2D, where a gradient strain field with higher strain near hetero-zone boundary and lower strain in zone interior is accommodated by the piling-up of a set of $\boldsymbol{b}\|x$ oriented dislocations, forming strain gradient $\frac{\partial \eta^p}{\partial x}x$. This assumption provides the GNDs configuration of a given strain state, thus enabling us to calculate the zone-scale σ_b by integrating the internal stress contribution of each dislocation that constitutes the gradient field [52,59,60].

Considering the $\frac{\partial \rho_{GND}}{\partial x}x$ component of a GNDs field, it is constituted by a set of $\boldsymbol{b}\|x$ oriented dislocations. Within this dislocation set, the full internal stress produced by the one located at (x, y) along z axis is

$$\sigma_{xx} = \frac{\mu b}{2\pi(1-\nu)}\frac{y\left(3x^2+y^2\right)}{\left(x^2+y^2\right)^2},\ \sigma_{xy} = -\frac{\mu b}{2\pi(1-\nu)}\frac{x\left(x^2-y^2\right)}{\left(x^2+y^2\right)^2},$$
$$\sigma_{yy} = -\frac{\mu b}{2\pi(1-\nu)}\frac{y\left(x^2-y^2\right)}{\left(x^2+y^2\right)^2},\ \sigma_{xz} = 0,$$
$$\sigma_{zz} = \frac{\mu b \nu}{\pi(1-\nu)}\frac{y}{x^2+y^2},\ \sigma_{yz} = 0. \tag{9}$$

Only dislocations within the spherical domain in radius of R $(x^2+y^2+z^2 \le R^2)$ are assumed to contribute to the net internal stress, since the contribution of distant dislocation is small, and the linear approximation assumed in Eq. (8) may no longer be valid for distant dislocations [52]. Therefore, integrating over the spherical domain, the net internal stress caused by this set of dislocations are

$$\sigma_{xx} = 0,\ \sigma_{xy} = -\frac{\mu b R^2}{8(1-\nu)}\frac{\partial \rho_{GND}}{\partial x},\ \sigma_{yy} = 0,\ \sigma_{xz} = 0,\ \sigma_{zz} = 0,\ \sigma_{yz} = 0 \tag{10-1}$$

Only the shear stress acted on the assumed slip plane is the effective net internal stress, i.e., the non-zero term, in which the negative sign indicates that the acting direction is opposite to the increase direction of ρ_{GND}. Applying similar considerations for the $\frac{\partial \rho_{GND}}{\partial y}y$ and $\frac{\partial \rho_{GND}}{\partial z}z$ components of GNDs field yields the other two non-zero internal stresses

$$\sigma_{yz} = -\frac{\mu b R^2}{8(1-\nu)}\frac{\partial \rho_{GND}}{\partial y}, \tag{10-2}$$

and

$$\sigma_{zx} = -\frac{\mu b R^2}{8(1-\nu)}\frac{\partial \rho_{GND}}{\partial z}. \tag{10-3}$$

Therefore, writing the net internal stresses in a von Mises form yields the effective σ_b

$$\sigma_b = \frac{\sqrt{3}}{8}\frac{\mu b R^2}{(1-\nu)}\sqrt{\left(\frac{\partial \rho_{GND}}{\partial x}\right)^2+\left(\frac{\partial \rho_{GND}}{\partial y}\right)^2+\left(\frac{\partial \rho_{GND}}{\partial z}\right)^2} \tag{11}$$

In a general deformation case, multiple slip systems are activated, and the strain gradient is not perfectly aligned with the assumed GNDs configuration. Therefore, it is necessary to implant a dislocation configuration correction coefficient k, yielding the zone-scale σ_b as

$$\sigma_b = \frac{\sqrt{3}}{8}\frac{\mu b k R^2}{(1-\nu)}\sqrt{\left(\frac{\partial \rho_{GND}}{\partial x}\right)^2+\left(\frac{\partial \rho_{GND}}{\partial y}\right)^2+\left(\frac{\partial \rho_{GND}}{\partial z}\right)^2} \tag{12}$$

The coefficient k may vary with the material properties.

In the FEM route, the global response of integrated heterostructure is calculated as the volume fraction-weighted sum of constituent zones. There may be several potential concerns for this deformation mechanism-based plasticity model. First, the intragranular back stress is ignored to make the model concise. This can be rationalized by the experimental observations that, in a homogeneous structure with only intragranular GNDs, the kinematic hardening and hysteresis effect are weak, especially as compared to that induced by zone-scale microstructure heterogeneity [6,23,40]. Second, the essence of assumed zone-scale GNDs configuration is to deploy three sets of mutually perpendicular dislocations to accommodate the 3D plastic strain gradient. Importantly, this model is potentially applicable for most structures with zone-scale heterogeneity if the constituent zones are properly partitioned and parameterized, since the derivation involves no restriction on microstructure configuration.

2.4. Parameterization & validation of the plasticity model

Considering the items of flow stress (Eq. (5)), the Hall-Petch description of yield strength in Cu is reliable until grain size drops to tens of nanometers [61]. The introduction of additional grain boundary-related annihilation term makes the Kocks-Mecking-Estrin model applicable to grains in submicron size [34,45]. The zone-scale back stress is not directly related to grain size. Therefore, the above constitutive model can be applied for the constituent zone with grain size ranging from hundreds of nanometers to tens of micrometers, which is exactly the case of common heterostructured Cu.

Table 1 lists the constitutive parameters for pure Cu. The microstructural and commonly used physical parameters, such as d,

Table 1
Constitutive parameters for Cu.

Parameters	Symbol	Value	Properties & access
Grain size (μm)	d	1–25 (CG), 0.1–1 (NS)	Microstructural, material and general physical parameters
Shear modulus (MPa)	μ	42,100	
Poissons ratio	υ	0.36	
Taylor constant	α	0.3 (CG), 0.26(NS)	
Burgers vector (μm)	b	0.000256	
Rate sensitivity exponent	m	20	
Lattice friction stress (MPa)	σ_0	25.5	
Hall-Petch slop (MPa $\cdot\,\mu$m$^{1/2}$)	k_{HP}	140	
Initial dislocation density (μm^{-2})	ρ_0	0.2 (CG), Varies according to material (NS)	
Saturation density of GNDs (μm^{-2})	ρ_{GND}^{max}	1000	
Geometric factor	k_1	0.15	SSDs evolution parameters, calibrated from the tensile response of homogeneous materials
Proportionality factor	k_2	0.011–0.02 (CG), 0.01 (NS)	
Dynamic recovery factor	k_3	2.38 (CG), 10.28 (NS)	
Reference strain rate (s^{-1})	$\dot{\varepsilon}_0$	1	
Dynamic recovery exponent	n_0	21.26	
Reference grain size (μm)	d_{ref}	0.7	
Effective radius of GNDs domain (μm)	R	0.8	calibrated from the response of heterostructures
GNDs configuration correction coefficient	k	0.68	

μ, etc., are taken according to material. The k_{HP} value (140 MPa $\cdot\,\mu$m$^{1/2}$) is the average value of those reported in literature, which are generally within 110–170 MPa $\cdot\,\mu$m$^{1/2}$. The maximum GND density experimentally examined near the CG/NS hetero-zone boundary is taken as the value of ρ_{GND}^{max} ($\sim 10^{15}\ m^{-2}$) [15]. The parameters controlling SSD evolution are partially obtained from literatures [34,36,40], and the others are determined by fitting the experimental results of homogeneous Cu with varying grain size (Fig. 3A and B).

The tension responses of a heterostructured Cu, with 25% CG (by volume fraction, d = 2 μm) dispersed in NS matrix (d = 0.24 μm) [5], is taken as a representative to calibrate the parameters describing back stress development. The FEM model used is exactly the dispersed model in Fig. 4, as introduced later. As the results compared in Fig. 3C and D, the simulated mechanical responses, including the strength, strain hardening, uniform elongation and even the strain localization development (the post-necking stage indicated by dotted line), are in good agreement with experimental measurements. Note that the appearance of apparent strength limit in simulated stress-strain curve indicates the development of strain localization. Since no specific damage criterion or instability source was prescribed in the model, the microstructure heterogeneity has to serve as the motivation of strain localization [7,49,62]. These results confirm that the deformation mechanism-based plasticity model established above is capable of providing quantitative description on the tensile behavior of heterostructure. With such confirmation, it will be used to simulate the behavior of heterostructured Cu with varying zone configurations and properties in the next sections, which helps us to probe the key microstructural factor controlling the synergistic responses.

3. Results

3.1. Effect of zone configuration

Structures consisting of multiple CG zones distributed in NS matrix in a clustered, lamellar or dispersed configuration are the most common heterostructures (Fig. 4), which can typically be prepared by partial recrystallization in severe plastically deformed NS bulks [5–7,20]. Here the FEM model of these three types of heterostructures are built with identical zone volume fraction (25% CG, Fig. 4), to probe the effects of zone configuration on synergistic mechanical responses. The grain size of CG and NS zones are taken as 2 μm and 0.24 μm, respectively.

The tensile properties of clustered heterostructures, in which the deformations mechanisms are selectively incorporated, are compared in Fig. 5A and B. Without any consideration on the effects of zone-scale deformation heterogeneity, i.e., the case with neither σ_b nor $\sigma_{Taylor,GND}$, the quick drop of strain hardening rate results in an extremely low uniform elongation (~4.4%), which actually is even smaller than the prediction by rule-of-mixture (~6%) [63]. The consideration of only $\sigma_{Taylor,GND}$ leads to a limited improvement in uniform elongation (~3%). In contrast, synergistic work hardening appears if both $\sigma_{Taylor,GND}$ and σ_b are incorporated (the shadow regions in Fig. 5B), resulting in a uniform elongation as large as ~20%. Such performance is consistent with experimental observations that a small fraction of recrystallization (generally <30%) in NS Cu matrix can effectively improve uniform elongation to near 20% or even reach 30%, at the yield strength level of >250 MPa [5,7–9]. This in turn proves the validity of the established constitutive model. Importantly, this comparison suggests that, the synergistic work hardening in heterostructure is primarily due to the back stress development and GND forest hardening [6,23,66].

Fig. 5C compares the tensile behavior of clustered, lamella and dispersed heterostructures. Interestingly, dispersed heterostructure exhibits higher work hardening and larger uniform elongation than the other two. The contribution of σ_b on flow stress is obtained by subtracting the response considering only $\sigma_{Taylor,GND}$ effect from the response incorporating both σ_b and $\sigma_{Taylor,GND}$ effects, and similar treatment produces the contribution of $\sigma_{Taylor,GND}$. As shown in Fig. 5D, the contribution of both σ_b and $\sigma_{Taylor,GND}$ are the highest in dispersed heterostructure and the lowest in clustered heterostructure. The hetero-zone boundary density appears as the most prominent microstructural difference enabled by the variation of zone configuration, which imply that the synergistic work hardening depends largely on hetero-zone boundary density. In other words, higher hetero-zone boundary density renders higher extra hardening from back stress and GNDs forest effect [3,14].

3.2. Hetero-zone boundary affected region (Hbar)

To probe the physical origin behind the dependence of synergistic mechanical responses on hetero-zone boundary density, the micromechanics are analyzed in terms of the zone-scale stress and strain gradient evolutions. Likewise, the clustered heterostructure is taken as a representative for analysis (Fig. 6A). A partition of the deformation stages is illustrated in Fig. 6B.

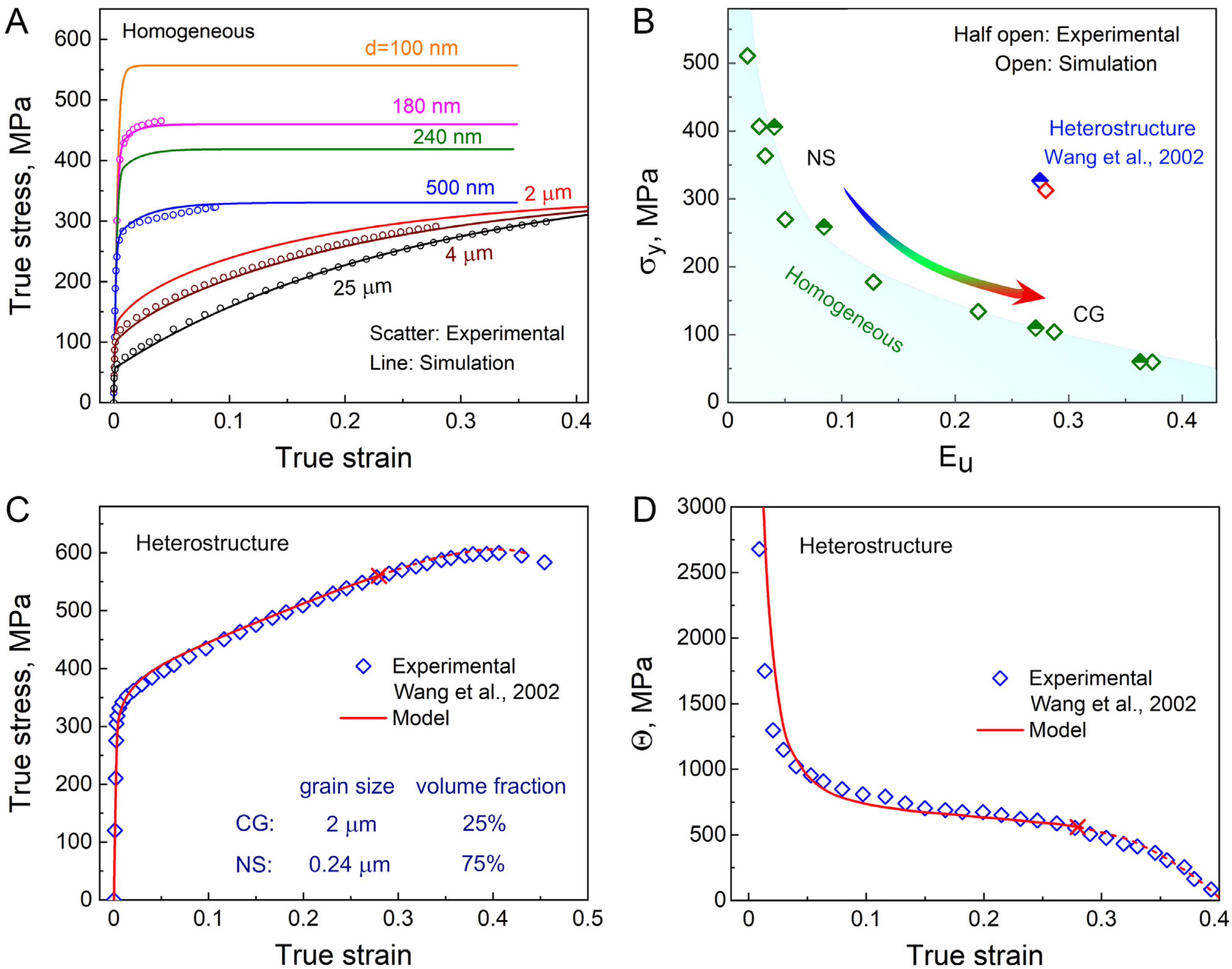

Fig. 3. Uniaxial tensile responses of (A, B) homogeneous Cu and (C, D) heterostructured Cu, comparing the model predictions (lines) with experimental measurements (scatters) [5,63–65], confirming the validity of the current plasticity model and the constitutive parameters used. σ_y, E_u and Θ represent the yield strength, uniform elongation and work hardening rate, respectively. Symbol $\times$ indicates the uniform elongation limit taken according to the Considère criterion.

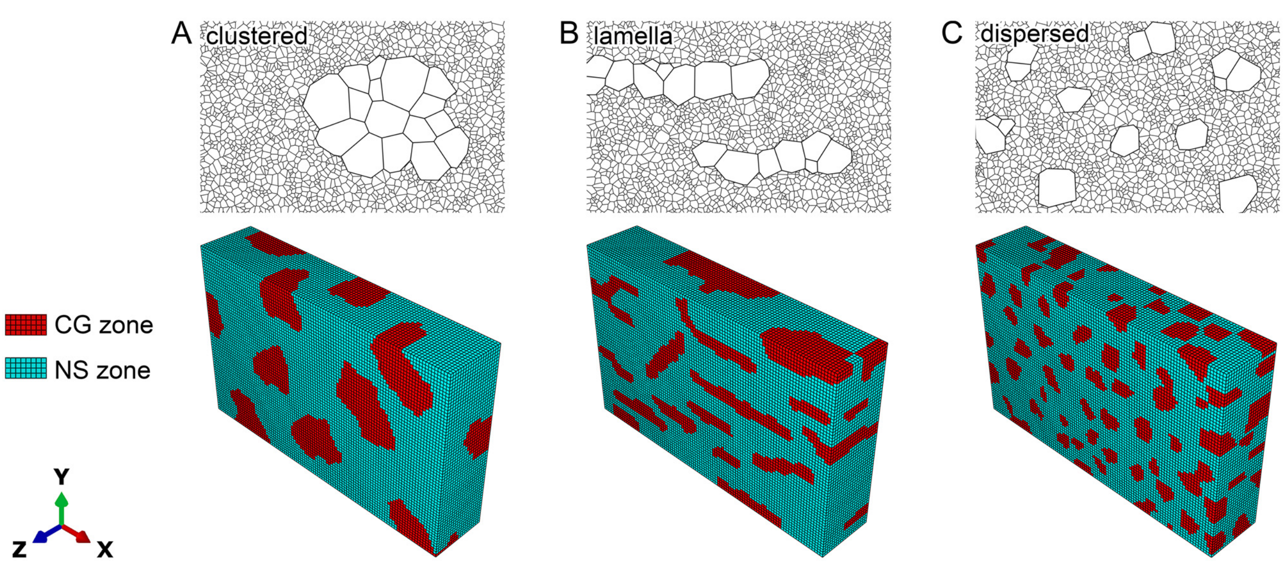

Fig. 4. Schematic and FEM model (representative volume element) of three types of heterostructures in Cu, with 25% CG zone distributed in NS matrix but varying zone configurations: (A) with clustered CG zone, (B) with lamellar CG zone, (C) CG dispersed in NS matrix. The ratio of the hetero-zone boundary density of three heterostructures is estimated to be 1:1.5:1.9. The model, in dimension of 80 μm $\times$ 50 μm $\times$ 16 μm, is meshed with C3D8 elements. Displacement of the bottom surface along Y is constrained, and the left and back surfaces have symmetrical constraints. Y is the loading direction of uniaxial tension.

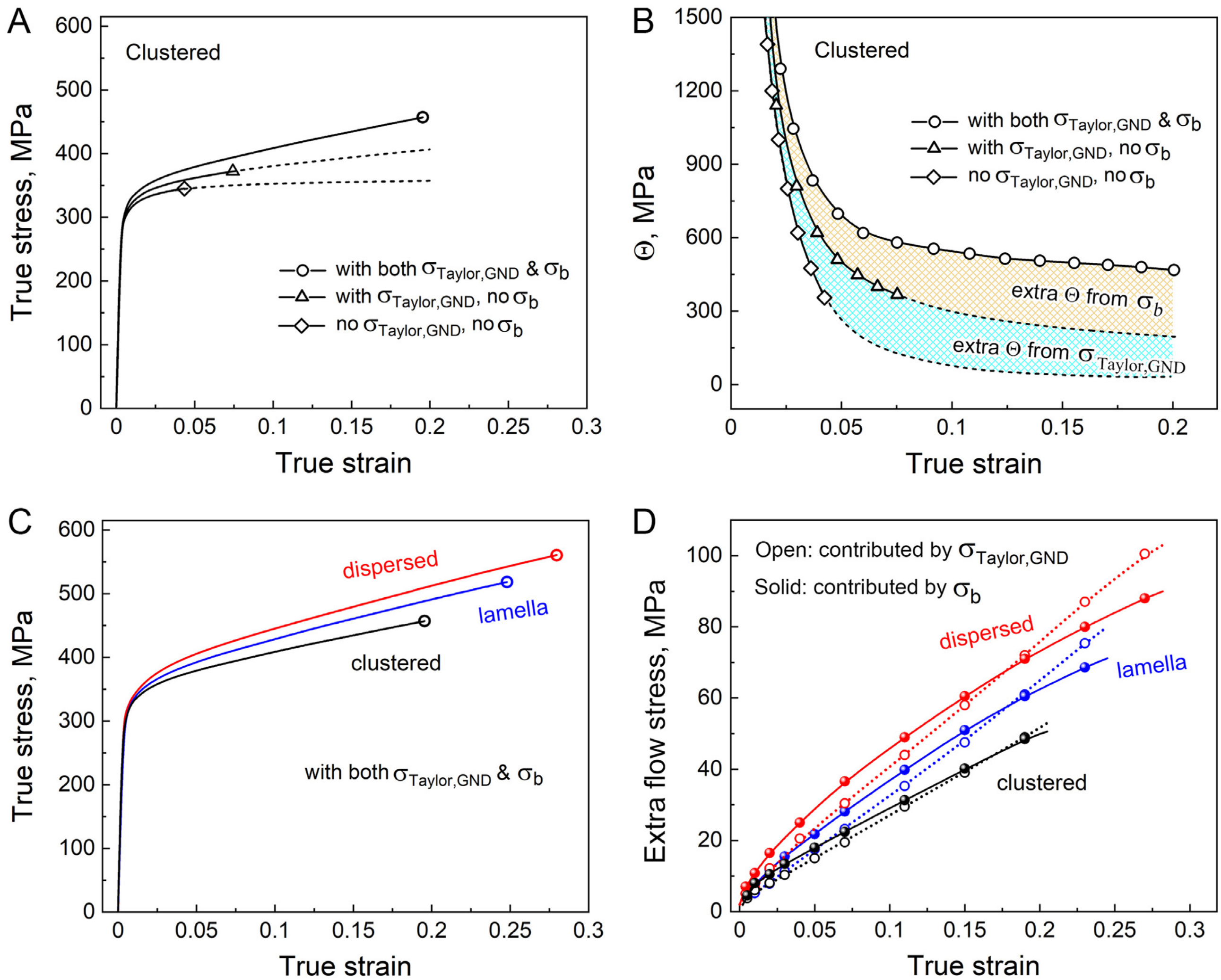

Fig. 5. Simulated mechanical response of heterostructures under uniaxial tension. (A) Stress-strain curves and (B) strain hardening rate of clustered heterostructure considering different hardening mechanisms. Comparison on the (C) stress-strain response and (D) extra flow stresses contributed by σ_b and $\sigma_{Taylor,GND}$, among three types of heterostructures. $\sigma_{Taylor,GND}$ represents the forest hardening effect of GNDs. In (A) and (C), the curves are truncated at the uniform elongation limit according to the Considère criterion.

The distribution and evolution of zone-scale von Mises stress, for the cases that σ_b and $\sigma_{Taylor,GND}$ are selectively considered, are presented in Fig. 6C–E. In the case in which neither σ_b nor $\sigma_{Taylor,GND}$ is considered, constituent zones are indifferent to the inter-zone deformation heterogeneity, other than the load partitioning (Fig. 6E). Interestingly, with the incorporation of σ_b and $\sigma_{Taylor,GND}$, significant local strengthening appears in the region near the zone boundary (Fig. 6C). The linear distribution across zone boundary (along path 1#) provides quantitative identification on the origin and development of extra local strengthening (Fig. 6F1–F3). In the fully elastic stage, no stress difference is observed among the three simulation cases. Additional von Mises stress contributed from σ_b and $\sigma_{Taylor,GND}$ starts to develop around zone boundaries upon entering the elastic-plastic transition stage (Fig. 6F1). In the stable plastic stage, the extra local strengthening increases continuously, and is higher at locations closer to the boundary (Fig. 6F2, F3). These observations confirm two critical physics for the effects of σ_b and $\sigma_{Taylor,GND}$. First, they mainly originate from the region near hetero-zone boundary, which leads to the boundary density dependence of synergistic work hardening (Fig. 5C and D). Second, they initiate at the elastic-plastic transition stage and increase with applied strain.

The development of σ_b and $\sigma_{Taylor,GND}$ lies in the accumulation of GNDs accompanying plastic strain gradient formation, which is needed to maintain inter-zone strain continuity [27,49]. As the maps and linear distributions shown in Fig. 7A and B, a plastic strain gradient peak starts to develop at boundary from the elastic-plastic transition stage and is largely enhanced at the uniform plastic stage. Since such extra strain gradient is produced by the deformation incompatibility-induced inter-zone interaction, the region across zone boundary with extra strain gradient is defined as the hetero-zone boundary affected region (Hbar, Fig. 7B and C) [14]. These observations indicate that extra back stress and GNDs forest hardening develop primarily from the Hbar. In other words, the Hbars are the origin of synergistic work hardening (Fig. 5). Moreover, the effects of zone configuration on synergistic work hardening may be attributed to the variation of Hbar volume fraction.

The strain gradient peak is fitted with Gaussian function to quantify the characteristic width (l_{Hbar}) and intensity (I) of Hbar (Fig. 7C). A statistical analysis reveals that the l_{Hbar} is on the order of a few micrometers, and it remains largely constant throughout the plastic stage (Fig. 7D and E). Interestingly, the simulated l_{Hbar}agrees well with the experimentally observed length of dislocations pileup at grain boundaries or zone boundaries [15,67]. The

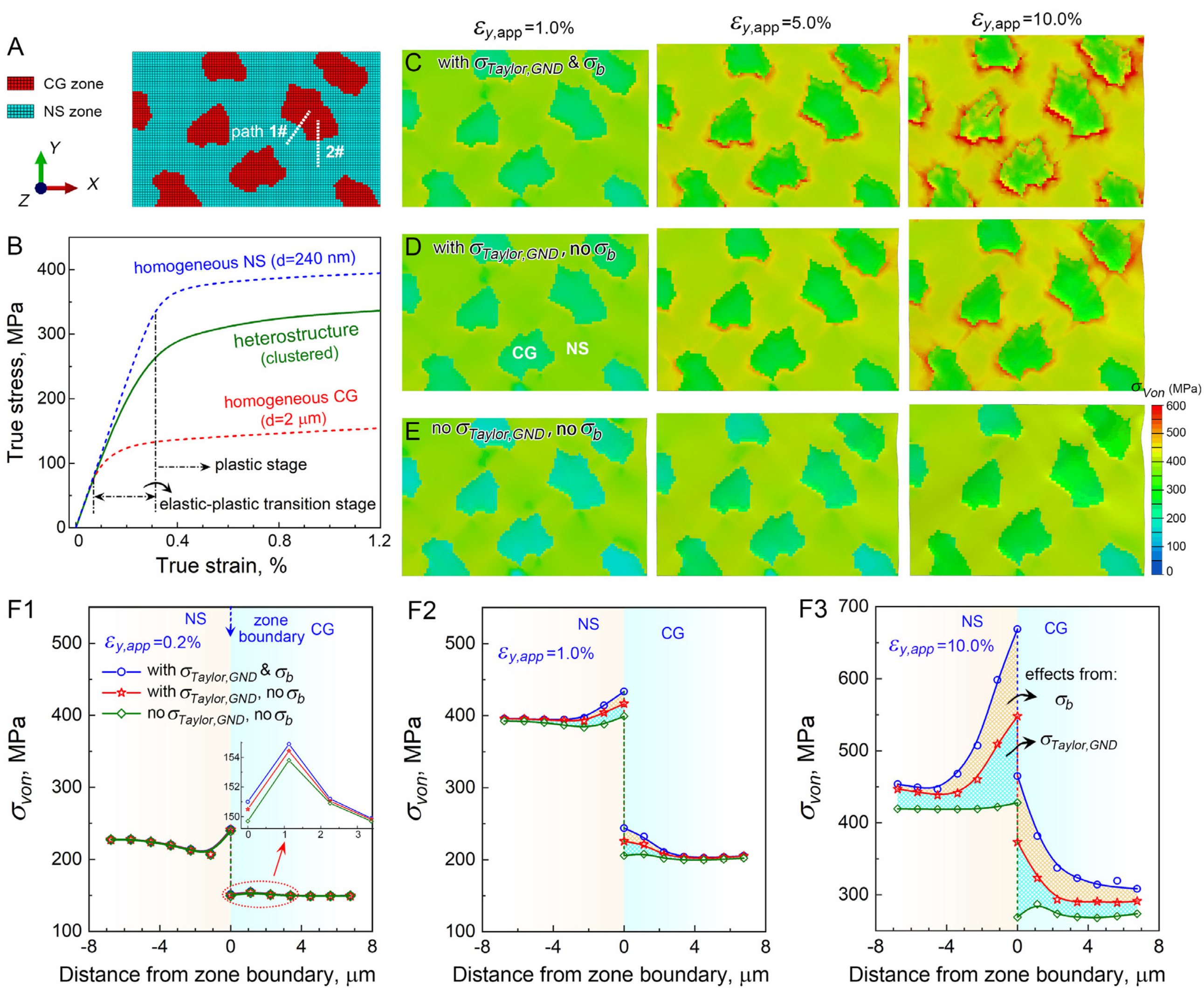

Fig. 6. Micromechanics at the hetero-zone boundary, analyzed by taking clustered heterostructure as a representative. (A) The FEM model showing the distribution of CG clusters and illustrating the paths selected perpendicular to boundary. (B) An illustration for the partition of strain stages of heterostructure. The distribution and evolution of zone-scale σ_{Von} in cases considering varying hardening mechanisms: (C) with both $\sigma_{Taylor,GND}$ and σ_b, (D) with $\sigma_{Taylor,GND}$ only, and (E) with neither $\sigma_{Taylor,GND}$ nor σ_b. Linear distribution of σ_{Von} along path 1# at the (F1) elastic-plastic transition stage, (F2) low plastic-strain stage, and (F3) high plastic-strain stage.

enhancement of *I* is due to the persistence of inter-zone deformation incompatibility and the resulting interaction. At the elastic-plastic transition stage, the difference in elastic limit activates elastic/plastic interaction and thus initiates plastic strain gradient [30,68]. Entering the plastic stage, the soft CG zone tends to sustain more plastic strain, which improves the inter-zone deformation incompatibility [6]. With increasing applied strain, CG zones remain plastically stable while the NS zone becomes unstable due to the exhaustion of strain hardening room, which activates plastically stable/unstable constraint to further enhance strain gradient [13,25].

3.3. Effect of mechanical incompatibility

The degree of mechanical incompatibility between constituent zones is a crucial factor that affects the Hbar behavior and consequently the synergistic mechanical responses [23,28,69]. Taking the clustered heterostructure as an example, the grain size of CG and NS zones varies in the range of 2–25 μm and 0.1–0.5 μm, respectively. As shown in Fig. 8A, the structure with largest grain size difference, i.e., with enhanced mechanical incompatibility, appears to exhibit the optimal strength-ductility balance with the highest work hardening. The results shown in Fig. 8B prove that higher work hardening from σ_b and $\sigma_{Taylor,GND}$ can be achieved as improving the mechanical incompatibility.

Fig. 9A and B compare the plastic strain gradient among heterostructures with varying mechanical incompatibility. Throughout the uniform elongation stage, the strain gradient intensity in the Hbar (at path 1#) increases continuously although the increasing rate is gradually decreased (Fig. 9C). This is in accordance with evolution of back stress effect (Figs. 5D and 8B), and may indicate a stronger inter-zone interaction at the low strain stage [23,70]. Moreover, larger mechanical incompatibility renders higher strain gradient in the Hbar (Fig. 9C). Interestingly, Hbar width slightly reduces with increasing mechanical incompatibility (Fig. 9D), which is in agreement with the experimental observation [56], but the underlying physics remain unclear.

A larger mechanical incompatibility enables larger deformation heterogeneity and stronger inter-zone interaction, thereby producing higher strain gradient in the Hbar [28,56]. Higher strain gradient developed in a narrower Hbar indicates the formation of a GNDs field with higher density gradient, which is expected to produce higher back stress and forest strengthening effects (Eq. (12)) [49,52]. In short, for engineering heterostructures, larger

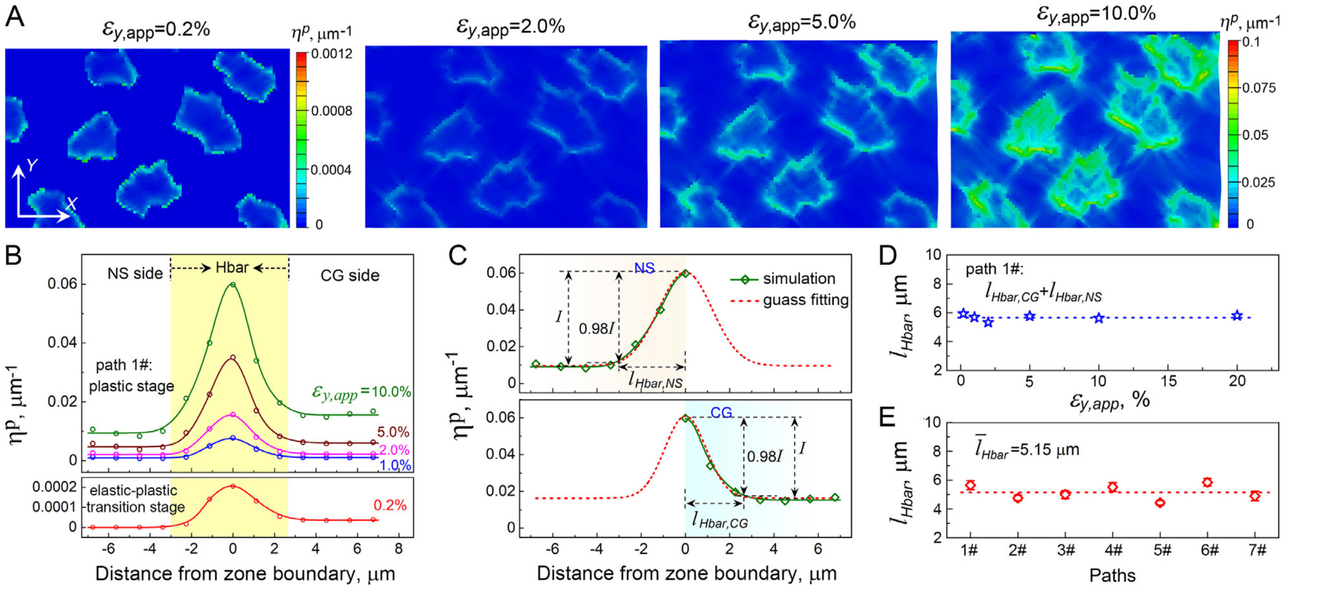

Fig. 7. Hetero-zone boundary affected region (Hbar) characterized by high plastic strain gradient η^p. The distribution and evolution of η^p: (A) maps, and (B) along path 1#. (C) Illustration of the characteristic width (l_{Hbar}) and strain gradient intensity (I) of Hbar. (D) The evolvement of l_{Hbar} with increasing applied strain $\varepsilon_{y,app}$. (E) The l_{Hbar} of several paths.

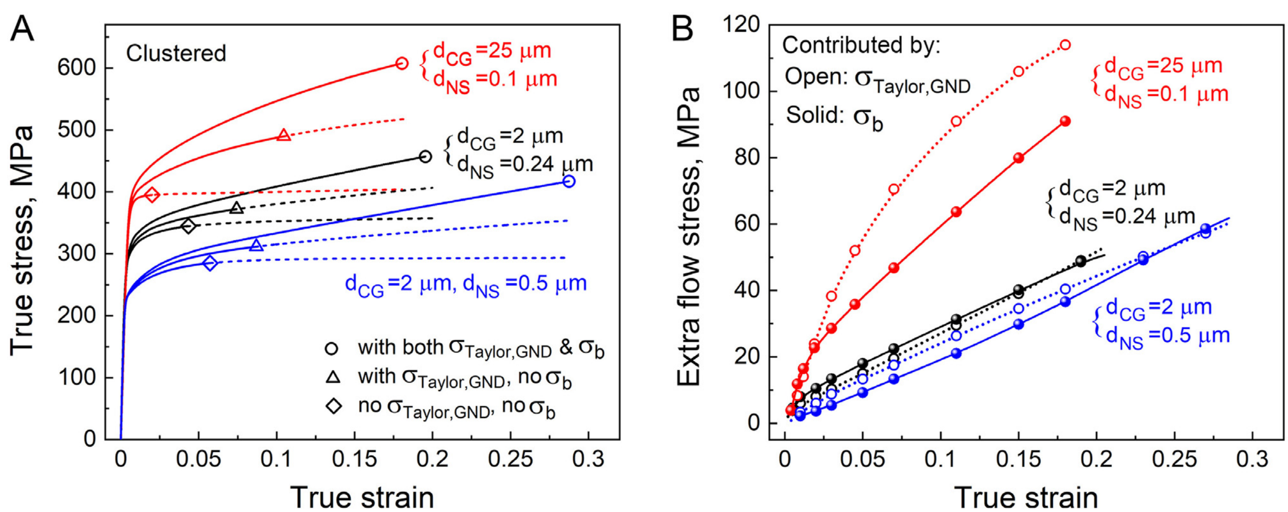

Fig. 8. Mechanical responses of clustered heterostructures with varying mechanical incompatibility between constituent zones: (A) stress-strain curves, (B) extra flow stress contributed by σ_b and $\sigma_{Taylor,GND}$.

mechanical incompatibility is expected to produce higher synergistic mechanical effects.

4. Discussion

4.1. Hbar-dominated synergistic work hardening

It is found that the zone-scale deformation heterogeneity is coordinated by forming Hbars characterized by strain gradient concentration (Fig. 7). Extra back stress and GNDs forest hardening develop in the Hbars (Fig. 6), thereby producing extra work hardening at macroscale (Fig. 5). These findings point out the mechanical essence of heterostructure design: building high-density hetero-zone boundaries to popularize strong strain gradient effects throughout the material [3,4]. There are two beliefs arising therefrom. First, for heterostructures with certain mechanical incompatibility, the synergistic work hardening should be dominated by the volume fraction of Hbars (V_{Hbar}). Second, Hbar may provide a unique microstructural perspective for seeking the quantitative relation between synergistic work hardening and microstructure heterogeneity.

Here the V_{Hbar} of clustered, lamellar and dispersed heterostructures are statistically evaluated as the volume fraction of regions within the 5.15 μm interval across zone boundaries, while the overlapping region between adjacent zone boundaries is calculated only once, i.e., $V_{Hbar} = \rho_{boundary} \times \bar{l}_{Hbar} - V_{Hbar,overlap}$. Surprisingly, the extra flow stresses $\Delta\sigma_f$ contributed from both σ_b and $\sigma_{Taylor,GND}$ are proportional to V_{Hbar} (Fig. 10A), i.e.

$$\Delta\sigma_f = k_{hardening} V_{Hbar}, \tag{13}$$

where $k_{hardening}$ represents the synergistic hardening efficiency of the Hbar. The experimental measurements in CG/NS laminates with varying layer thickness is reanalyzed [14,56], which reveals a similar linear relation between $\Delta\sigma_f$ and V_{Hbar} (Fig. 10B). Such explicit-yet-convincing relationship confirms the above beliefs and proves the key role of Hbar in synergistic work hardening.

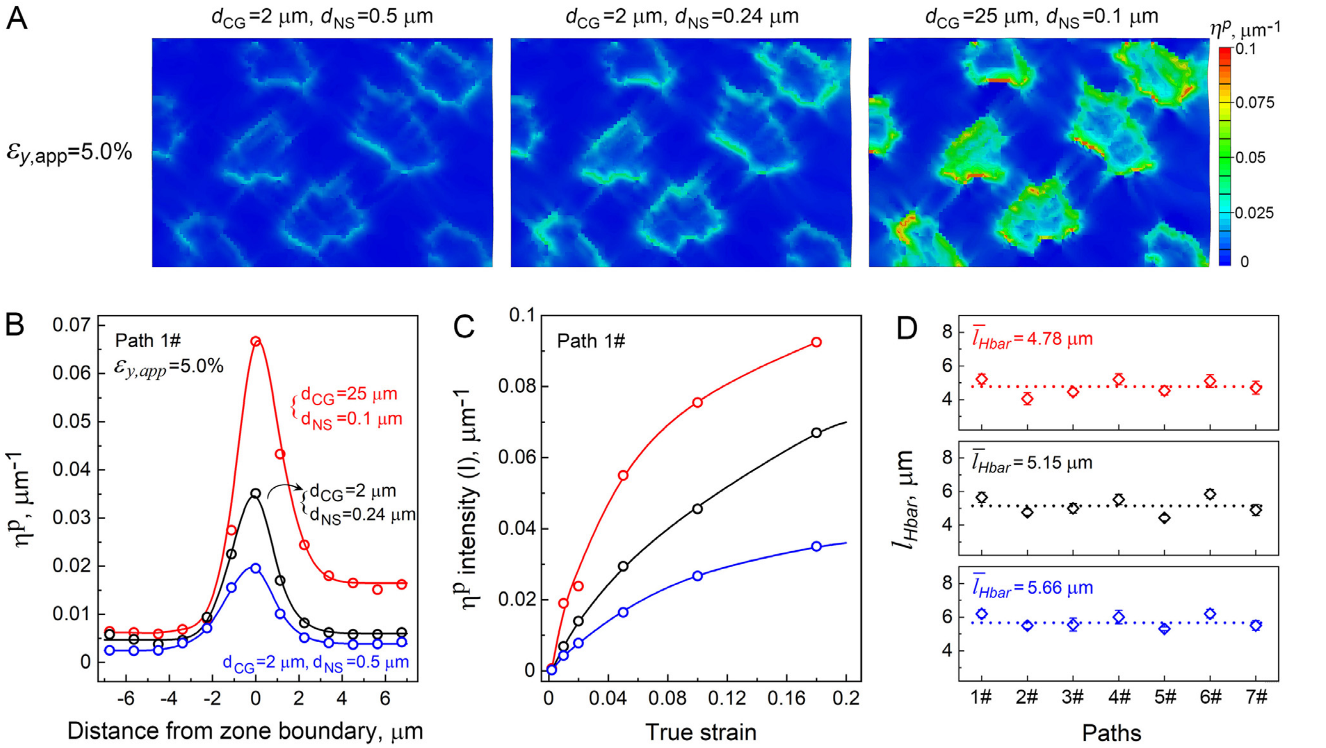

Fig. 9. Comparison on the Hbar behavior among three clustered heterostructures with varying mechanical incompatibility. (A) Maps of the zone-scale plastic strain gradient η^p at the applied strain of 5.0%. (B) Linear distribution of η^p along Path 1#. (C) Evolution of the η^p intensity in the Hbar identified by Path 1#. (D) The characteristic width of Hbars. In (B–D), data with the same color originate from the same heterostructure. For instance, the red data are obtained from the heterostructure composed of 2 μm-diameter CG and 0.1 μm-diameter NS.

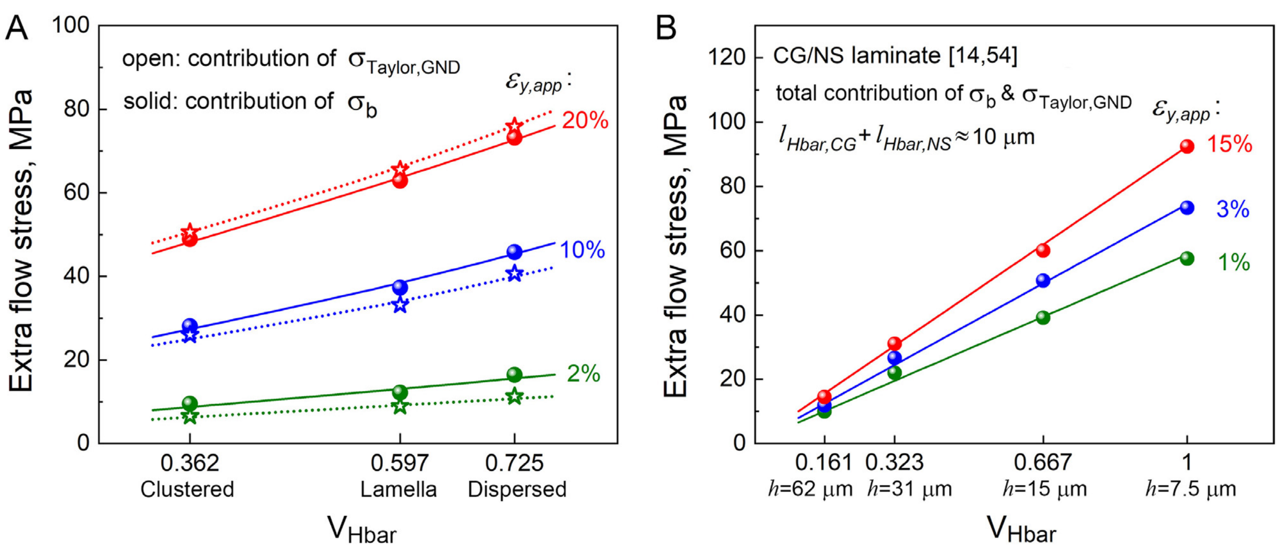

Fig. 10. (A) The extra flow stress (data in Fig. 5D) plotted as a function of V_{Hbar}, obtaining a linear relationship. (B) Similar linear relationship in CG/NS laminates with varying layer thickness h, obtained by re-analyzing the experimentally measured stress-strain curves, microstructure and zone-scale strain distributions [14,56].

Note that, in the case without Hbar overlapping, V_{Hbar} is inversely proportional to the average spacing h of heterogeneous zones, thus a Hall-Petch-like expression $\Delta\sigma_f = k'_{hardening} h^{-\frac{1}{2}}$ is met. However, for most practical heterostructures, such as that prepared by partial recrystallization, Hbar overlapping may occur, since the configuration and distribution of constituent zones are difficult to be precisely controlled [20]. The Hall-Petch-like expression would overestimate the synergistic mechanical response. While V_{Hbar} is a microstructural parameter incorporating the effects of the configuration and distribution of zones as well as the characteristic width of Hbar that determined by material properties and mechanical incompatibility. In this regard, V_{Hbar} would be a more adaptable parameter, enabling a physical-based yet simple quantification on the synergistic work hardening.

4.2. Strength-ductility combination optimized by Hbar

The dominant role of Hbar in synergistic work hardening has significant implications in the design of heterostructures for superior strength-ductility combination. The key principle is to maximize the strain gradient-dependent back stress and GND forest hardening. As suggested by Eq. (13), the strategies that have been

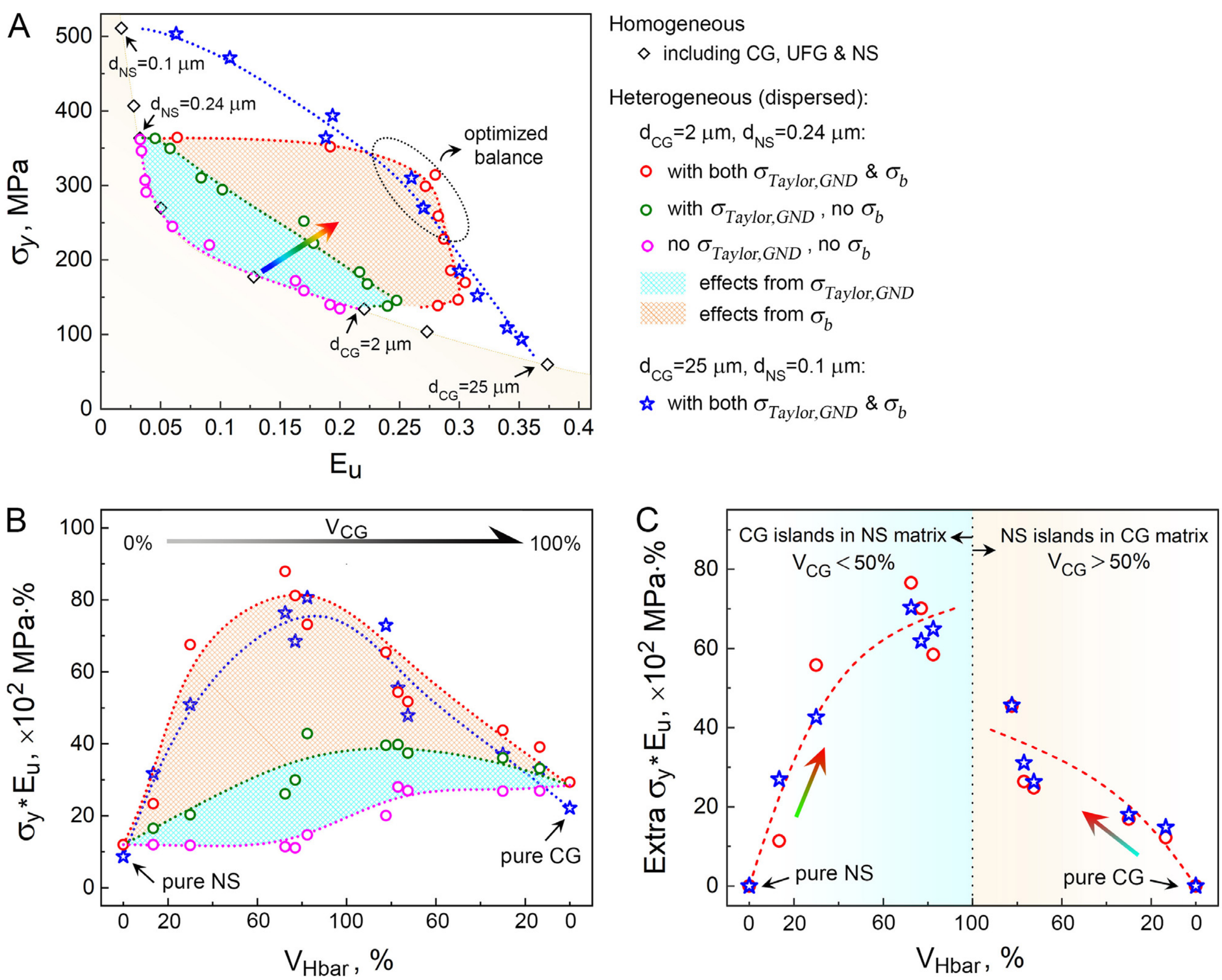

Fig. 11. Strength-ductility combination optimized by Hbar in dispersed heterostructure. (A) The combination of σ_y and E_u in heterostructures with varying volume fraction of CG zones (V_{CG}). The performances of homogeneous structures are also provided for comparison. (B) $\sigma_y * E_u$ versus V_{Hbar}. (C) Extra $\sigma_y * E_u$ versus V_{Hbar}. Extra $\sigma_y * E_u$ is the $\sigma_y * E_u$ increment contributed by σ_b and $\sigma_{Taylor,GND}$. Three subgraphs share the legend on the right of (A).

ready are to improve the V_{Hbar} or the $k_{hardening}$. In addition to manipulating zone configuration, an easy-to-implement route for improving the V_{Hbar} is tuning the volume fraction of constituent zones [10,70]. Higher $k_{hardening}$ value indicates greater plastic strain gradient in the Hbars, which can be achieved by properly increasing the inter-zone mechanical incompatibility (Figs. 8 and 9) or by selecting materials with medium/low stacking fault energy to facilitate GND piling-up [28,56,59].

Fig. 11A presents the strength-ductility map of dispersed heterostructures with the volume fraction of CG varying within 0–100%. It reveals the achievement of optimized strength-ductility combinations, with ~25% uniform elongation at the yield strength level of > 200 MPa, which evades the conventional trade-off dilemma. We take the product of yield strength and uniform elongation ($\sigma_y * E_u$) as an indicator of strength-ductility combination and plot it as a function of V_{Hbar} (Fig. 11B). It is found that the optimal strength-ductility combination (with maximum $\sigma_y * E_u$) actually occurs as V_{Hbar} approaches saturation. Fig. 11C reveals that the larger the V_{Hbar}, the higher the extra $\sigma_y * E_u$ contributed by the σ_b and $\sigma_{Taylor,GND}$. These results prove the key role of Hbar in optimizing strength-ductility synergy [14,15].

Several points need to be addressed. First, in several cases enhanced mechanical incompatibility do not appear to display better strength-ductility combination (Fig. 11). This is due to the selection of extremely refined grain for NS zone ($d_{NS} = 0.1\ \mu m$). Finer grains in NS zone produces improved flow stress, which demands much higher strain hardening to maintain elongation uniformity, thereby rendering a medium uniform elongation although the Hbar effects are indeed enhanced (Fig. 8). Second, it was found that strength-ductility combination is largely affected by the limit of GNDs density ρ_{GND}^{max} in Hbar. Therefore, constituent zones should be selected with higher capability in GNDs accommodation [22]. Moreover, in the cases with identical V_{Hbar}, the heterostructure with CG zones embedded in NS matrix enables higher synergistic mechanical effects than the heterostructure with NS zones embedded in CG matrix, as evidenced in Fig. 11C. This implies that microstructure configuration also affects the intensity of inter-zone interaction [16], in addition to the V_{Hbar}.

As analyzed above, the direct effect of zone configuration, mechanical incompatibility and zone content lies in affecting the Hbar, either on the volume fraction or on the hardening efficiency or even both, while the extra work hardening originates primarily in the Hbar. Therefore, the Hbar can be considered as a unified microstructural factor that controls the extra work hardening of heterostructure.

These fundamentals on Hbar, after systematic experimental validation, is expected to help guide future innovation in microstructure design towards superior strength-ductility synergy. Note that, similar to most existing deformation analysis [6,39,52,53], the forward stress, which acts in the same direction of applied stress in the region in front of GNDs pile-up [66,71], is not considered here. Because the physics behind it is not yet fully understood, and it is currently difficult to incorporate it into the constitutive model. However, the extraordinary mechanical properties of heterostructures observed experimentally suggests that the back stress and forward stress collectively produce net hardening effect, named hetero-deformation induced (HDI) hardening [56,66]. In other words, in monotonic tension, the hardening effect of back stress should be stronger than the softening effect of forward stress. In addition, both of them are generated by the GND pile-ups in Hbar. These lead us to believe that the HDI stress should be positively correlated with the back stress. Therefore, the neglect of forward stress does not affect current exploration and discussion on the key microstructure factor controlling synergistic work hardening. The physics and constitutive law of forward stress remain to be systematic studied.

5. Conclusions

Taking heterostructured Cu as a model material, the effect of microstructural factors on the synergistic mechanical responses and micromechanics of heterostructure has been investigated with the aid of constitutive modeling. Special attention was devoted to seeking the origin, the unified controlling factor and the microstructure-based quantitative evaluation of extra work hardening. The main findings are:

(i) A deformation mechanism-based plasticity model is proposed, which incorporates the zone-scale deformation heterogeneity-induced back stress by integrating the long-range internal stress of GNDs field. It can provide good predictions on the tensile behavior of heterostructure.
(ii) Inter-zone interaction induces the formation of a hetero-zone boundary affected region (Hbar), which is characterized by high strain gradient concentration. The extra work hardening originates primarily in the Hbar, due to the development of extra back stress and GNDs forest hardening.
(iii) Hbar unifies the effects of zone configuration, mechanical incompatibility and zone volume fraction, which plays the key role in controlling synergistic work hardening and optimizing strength-ductility combination. Specifically, the extra flow stress caused by synergistic work hardening increases proportionally with the volume fraction of the Hbar, i.e., $\Delta\sigma_f = k_{hardening}V_{Hbar}$, and optimal strength-ductility combination is achieved as V_{Hbar} approaches saturation.
(iv) The key principle of optimizing strength-ductility combination is to maximize the Hbar effects. The possible routes include increasing V_{Hbar} by building dispersed zone configuration and tuning zone volume fraction, enhancing the hardening efficiency of Hbar ($k_{hardening}$) by improving mechanical incompatibility, and adopting the microstructure configuration with soft zones distributed in hard matrix rather than the opposite.

Declaration of Competing Interest

The authors declare that they have no known competing financial interests or personal relationships that could have appeared to influence the work reported in this paper.

Acknowledgments

This work was supported by the NSFC Programs (Nos. 1210020469, 51931003, 11890681, 12032001 & 11521202), the Postdoctoral Science Foundation of China (Nos. 2020M680223 & BX2021011), and the Hong Kong Research Grants Council (GRF 11214121).

References

[1] K. Lu, Making strong nanomaterials ductile with gradients, Science 345 (2014) 1455–1456.
[2] M.A. Meyers, A. Mishra, D.J. Benson, Mechanical properties of nanocrystalline materials, Prog. Mater. Sci. 51 (2006) 427–556.
[3] X.L. Wu, Y.T. Zhu, Heterogeneous materials: a new class of materials with unprecedented mechanical properties, Mater. Res. Lett. 5 (2017) 527–532.
[4] Y.T. Zhu, K. Ameyama, P.M. Anderson, I.J. Beyerlein, H.J. Gao, H.S. Kim, E. Lavernia, S. Mathaudhu, H. Muhrabi, R.O. Ritchie, N. Tsuji, X.Y. Zhang, X.L. Wu, Heterostructured materials: superior properties from hetero-zone interaction, Mater. Res. Lett. 9 (2021) 1–31.
[5] Y.M. Wang, M.W. Chen, F.H. Zhou, E. Ma, High tensile ductility in a nanostructured metal, Nature 419 (2002) 912–915.
[6] X.L. Wu, M.X. Yang, F.P. Yuan, G.L. Wu, Y.J. Wei, X.X. Huang, Y.T. Zhu, Heterogeneous lamella structure unites ultrafine-grain strength with coarse-grain ductility, Proc. Natl. Acad. Sci. USA 112 (2015) 14501–14505.
[7] Y.F. Wang, C.X. Huang, Q. He, F.J. Guo, M.S. Wang, L.Y. Song, Y.T. Zhu, Heterostructure induced dispersive shear bands in heterostructured Cu, Scr. Mater. 170 (2019) 76–80.
[8] Y.H. Zhao, T. Topping, Y. Li, E.J. Lavernia, Strength and ductility of Bi-modal Cu, Adv. Eng. Mater. 13 (2011) 865–871.
[9] C.X. Ren, Q. Wang, Z.J. Zhang, H.J. Yang, Z.F. Zhang, Surface strengthening behaviors of pure Cu with heterogeneous microstructures, Mater. Sci. Eng. A 727 (2018) 192–199.
[10] Z. Cheng, H.F. Zhou, Q.H. Lu, H.J. Gao, L. Lu, Extra strengthening and work hardening in gradient nanotwinned metals, Science 362 (2018) eaau1925.
[11] X.Y. Li, L. Lu, J.G. Li, X. Zhang, H.J. Gao, Mechanical properties and deformation mechanisms of gradient nanostructured metals and alloys, Nat. Rev. Mater. 5 (2020) 706–723.
[12] Y. Lin, J. Pan, H.F. Zhou, H.J. Gao, Y. Li, Mechanical properties and optimal grain size distribution profile of gradient grained nickel, Acta Mater. 153 (2018) 279–289.
[13] X.L. Wu, P. Jiang, L. Chen, F.P. Yuan, Y.T. Zhu, Extraordinary strain hardening by gradient structure, Proc. Natl. Acad. Sci. USA 111 (2014) 7197–7201, doi:10.1073/pnas.1324069111.
[14] C.X. Huang, Y.F. Wang, X.L. Ma, S. Yin, H.W. Höppel, M. Göken, X.L. Wu, H.J. Gao, Y.T. Zhu, Interface affected zone for optimal strength and ductility in heterogeneous laminate, Mater. Today 21 (2018) 713–719.
[15] X.L. Ma, C.X. Huang, J. Moering, M. Ruppert, H.W. Höppel, M. Göken, J. Narayan, Y.T. Zhu, Mechanical properties of copper/bronze laminates: role of interfaces, Acta Mater. 116 (2016) 43–52.
[16] M. Huang, C. Xu, G.H. Fan, E. Maawad, W.M. Gan, L. Geng, F.X. Lin, G.Z. Tang, H. Wu, Y. Du, D.Y. Li, K.S. Miao, T.T. Zhang, X.S. Yang, Y.P. Xia, G.J. Cao, H.J. Kang, T.M. Wang, T.Q. Xiao, H.L. Xie, Role of layered structure in ductility improvement of layered Ti-Al metal composite, Acta Mater. 153 (2018) 235–249.
[17] H. Wu, G.H. Fan, M. Huang, L. Geng, X.P. Cui, H.L. Xie, Deformation behavior of brittle/ductile multilayered composites under interface constraint effect, Int. J. Plast. 89 (2017) 96–109.
[18] H.K. Park, K. Ameyama, J. Yoo, H. Hwang, H.S. Kim, Additional hardening in harmonic structured materials by strain partitioning and back stress, Mater. Res. Lett. 6 (2018) 261–267.
[19] S.K. Vajpai, M. Ota, Z. Zhang, K. Ameyama, Three-dimensionally gradient harmonic structure design: an integrated approach for high performance structural materials, Mater. Res. Lett. 4 (2016) 191–197.
[20] P. Sathiyamoorthi, H.S. Kim, High-entropy alloys with heterogeneous microstructure: processing and mechanical properties, Prog. Mater. Sci. 123 (2020) 100709.
[21] Y.M. Zhang, C.Y. Wang, K.M. Reddy, W. Li, X.D. Wang, Study on the deformation mechanism of a high-nitrogen duplex stainless steel with excellent mechanical properties originated from bimodal grain design, Acta Mater. 226 (2022) 117670.
[22] Y.F. Wang, M.S. Wang, X.T. Fang, F.J. Guo, H.Q. Liu, R.O. Scattergood, C.X. Huang, Y.T. Zhu, Extra strengthening in a coarse/ultrafine grained laminate: role of gradient interfaces, Int. J. Plast. 123 (2019) 196–207.
[23] Y.F. Wang, M.X. Yang, X.L. Ma, M.S. Wang, K. Yin, A.H. Huang, C.X. Huang, Improved back stress and synergetic strain hardening in coarse–grain/nanostructure laminates, Mater. Sci. Eng. A 727 (2018) 113–118.
[24] Y.F. Wang, C.X. Huang, M.S. Wang, Y.S. Li, Y.T. Zhu, Quantifying the synergetic strengthening in gradient material, Scr. Mater. 150 (2018) 22–25.
[25] Y.F. Wang, Y.T. Zhu, X.L. Wu, Y.G. Wei, C.X. Huang, Inter-zone constraint modifies the stress-strain response of the constituent layer in gradient structure, Sci. China Mater. 64 (2021) 3114–3123.
[26] J. Wang, A. Misra, An overview of interface-dominated deformation mechanisms in metallic multilayers, Curr. Opin. Solid State Mater. Sci. 15 (2011) 20–28.
[27] H. Mughrabi, Dual role of deformation-induced geometrically necessary dislocations with respect to lattice plane misorientations and/or long-range internal stresses☆, Acta Mater. 54 (2006) 3417–3427.
[28] T. Wan, Z. Cheng, L.F. Bu, L. Lu, Work hardening discrepancy designing to strengthening gradient nanotwinned Cu, Scr. Mater. 201 (2021) 113975.

[29] X.L. Wu, P. Jiang, L. Chen, J.F. Zhang, F.P. Yuan, Y.T. Zhu, Synergetic strengthening by gradient structure, Mater. Res. Lett. 2 (2014) 185–191.
[30] Y.F. Wang, C.X. Huang, Z.K. Li, X.T. Fang, M.S. Wang, Q. He, F.J. Guo, Y.T. Zhu, Shear band stability and uniform elongation of gradient structured material: role of lateral constraint, Extrem. Mech. Lett. 37 (2020) 100686.
[31] L.L. Zhu, S.Q. Shi, K. Lu, J. Lu, A statistical model for predicting the mechanical properties of nanostructured metals with bimodal grain size distribution, Acta Mater. 60 (2012) 5762–5772.
[32] L.L. Zhu, J. Lu, Modelling the plastic deformation of nanostructured metals with bimodal grain size distribution, Int. J. Plast. 30-31 (2012) 166–184.
[33] L.L. Zhu, H.H. Ruan, A.Y. Chen, X. Guo, J. Lu, Microstructures-based constitutive analysis for mechanical properties of gradient-nanostructured 304 stainless steels, Acta Mater. 128 (2017) 375–390.
[34] J.J. Li, A.K. Soh, Modeling of the plastic deformation of nanostructured materials with grain size gradient, Int. J. Plast. 39 (2012) 88–102.
[35] J.J. Li, S.H. Chen, X.L. Wu, A.K. Soh, A physical model revealing strong strain hardening in nano-grained metals induced by grain size gradient structure, Mater. Sci. Eng. A 620 (2015) 16–21.
[36] J.F. Zhao, Q.H. Kan, L.C. Zhou, G.Z. Kang, H.D. Fan, X. Zhang, Deformation mechanisms based constitutive modelling and strength-ductility mapping of gradient nano-grained materials, Mater. Sci. Eng. A 742 (2019) 400–408.
[37] J. Liu, J. Li, G. Dirras, K. Ameyama, F. Cazes, M. Ota, A three-dimensional multi-scale polycrystalline plasticity model coupled with damage for pure Ti with harmonic structure design, Int. J. Plast. 100 (2018) 192–207.
[38] M. Delincé, Y. Bréchet, J.D. Embury, M.G.D. Geers, P.J. Jacques, T. Pardoen, Structure–property optimization of ultrafine-grained dual-phase steels using a microstructure-based strain hardening model, Acta Mater. 55 (2007) 2337–2350.
[39] J.J. Li, G.J. Weng, S.H. Chen, X.L. Wu, On strain hardening mechanism in gradient nanostructures, Int. J. Plast. 88 (2017) 89–107.
[40] J.J. Li, W.J. Lu, S.H. Chen, C.H. Liu, Revealing extra strengthening and strain hardening in heterogeneous two-phase nanostructures, Int. J. Plast. 126 (2020) 102626.
[41] J.J. Li, S.H. Chen, G.J. Weng, W.J. Lu, A micromechanical model for heterogeneous nanograined metals with shape effect of inclusions and geometrically necessary dislocation pileups at the domain boundary, Int. J. Plast. 144 (2021) 103024.
[42] J.F. Zhao, X.C. Lu, F.P. Yuan, Q.H. Kan, S.X. Qu, G.Z. Kang, X. Zhang, Multiple mechanism based constitutive modeling of gradient nanograined material, Int. J. Plast. 125 (2020) 314–330.
[43] J.F. Zhao, M. Zaiser, X.C. Lu, B. Zhang, C.X. Huang, G.Z. Kang, X. Zhang, Size-dependent plasticity of hetero-structured laminates: a constitutive model considering deformation heterogeneities, Int. J. Plast. 145 (2021) 103063.
[44] H. Mecking, U.F. Kocks, Kinetics of flow and strain-hardening, Acta Metall. 29 (1981) 1865–1875.
[45] Y. Estrin, A.S. Krausz, K. Krausz, Dislocation-density-related constitutive modeling, in: Unified Constitutive Laws of Plastic Deformation, Academic Press, San Diego, 1996, pp. 69–109.
[46] Y. Estrin, H. Mecking, A unified phenomenological description of work hardening and creep based on one-parameter models, Acta Metall. 32 (1984) 57–70.
[47] U.F. Kocks, H. Mecking, Physics and phenomenology of strain hardening: the FCC case, Prog. Mater. Sci. 48 (2003) 171–273.
[48] Y. Huang, S. Qu, K.C. Hwang, M. Li, H. Gao, A conventional theory of mechanism-based strain gradient plasticity, Int. J. Plast. 20 (2004) 753–782.
[49] M.F. Ashby, The deformation of plastically non-homogeneous materials, Philos. Mag. 21 (1970) 399–424.
[50] H. Gao, Y. Huang, W.D. Nix, J.W. Hutchinson, Mechanism-based strain gradient plasticity-I. Theory, J. Mech. Phys. Solids 47 (1999) 1239–1263.
[51] H.J. Gao, Y.G. Huang, Geometrically necessary dislocation and size-dependent plasticity, Scr. Mater. 48 (2003) 113–118.
[52] C.J. Bayley, W.A.M. Brekelmans, M.G.D. Geers, A comparison of dislocation induced back stress formulations in strain gradient crystal plasticity, Int. J. Solids Struct. 43 (2006) 7268–7286.
[53] H. Mughrabi, Dislocation wall and cell structures and long-range internal stresses in deformed metal crystals, Acta Metall. 31 (1983) 1367–1379.
[54] J.W. Hutchinson, N.A. Fleck, Strain gradient plasticity, in: Advances in Applied Mechanics, Elsevier, 1997, pp. 295–361.
[55] J.F. Nye, Some geometrical relations in dislocated crystals, Acta Metall. 1 (1953) 153–162.
[56] Y.F. Wang, C.X. Huang, X.T. Fang, H.W. Höppel, M. Göken, Y.T. Zhu, Hetero-deformation induced (HDI) hardening does not increase linearly with strain gradient, Scr. Mater. 174 (2020) 19–23.
[57] H. Zhou, C.X. Huang, X.C. Sha, L.R. Xiao, X.L. Ma, H.W. Höppel, M. Göken, X.L. Wu, K. Ameyama, X.D. Han, Y.T. Zhu, *In-situ* observation of dislocation dynamics near heterostructured interfaces, Mater. Res. Lett. 7 (2019) 376–382.
[58] E.C. Oliver, M.R. Daymond, P.J. Withers, Interphase and intergranular stress generation in carbon steels, Acta Mater. 52 (2004) 1937–1951.
[59] J.P. Hirth, J. Lothe, Dislocation pileups, in: Theory of Dislocations, 2nd ed., Wiley, New York, 1982, pp. 765–790.
[60] T.E. Mitchell, The stress-fields around groups of dislocations in face-centred cubic metals, Philos. Mag. 10 (1964) 301–314.
[61] J. Chen, L. Lu, K. Lu, Hardness and strain rate sensitivity of nanocrystalline Cu, Scr. Mater. 54 (2006) 1913–1918.
[62] X. Sun, K.S. Choi, W.N. Liu, M.A. Khaleel, Predicting failure modes and ductility of dual phase steels using plastic strain localization, Int. J. Plast. 25 (2009) 1888–1909.
[63] X.L. Ma, C.X. Huang, W.Z. Xu, H. Zhou, X.L. Wu, Y.T. Zhu, Strain hardening and ductility in a coarse-grain/nanostructure laminate material, Scr. Mater. 103 (2015) 57–60.
[64] Y.F. Wang, F.J. Guo, Q. He, L.Y. Song, M.S. Wang, A.H. Huang, Y.S. Li, C.X. Huang, Synergetic deformation-induced extraordinary softening and hardening in gradient copper, Mater. Sci. Eng. A 752 (2019) 217–222.
[65] Y.F. Wang, M.S. Wang, K. Yin, A.H. Huang, Y.S. Li, C.X. Huang, Yielding and fracture behaviors of coarse-grain/ultrafine-grain heterogeneous-structured copper with transitional interface, Trans. Nonferr. Metal. Soc. 29 (2019) 588–594.
[66] Y.T. Zhu, X.L. Wu, Perspective on hetero-deformation induced (HDI) hardening and back stress, Mater. Res. Lett. 7 (2019) 393–398.
[67] L.E. Murr, Dislocation ledge sources: dispelling the myth of Frank–Read source importance, Metall. Mater. Trans. A 47 (2016) 5811–5826.
[68] Z. Zeng, X.Y. Li, D.S. Xu, L. Lu, H.J. Gao, T. Zhu, Gradient plasticity in gradient nano-grained metals, Extrem. Mech. Lett. 8 (2016) 213–219.
[69] T.H. Fang, W.L. Li, N.R. Tao, K. Lu, Revealing extraordinary intrinsic tensile plasticity in gradient nano-grained copper, Science 331 (2011) 1587–1590.
[70] X.T. Fang, G.Z. He, C. Zheng, X.L. Ma, D. Kaoumi, Y.S. Li, Y.T. Zhu, Effect of heterostructure and hetero-deformation induced hardening on the strength and ductility of brass, Acta Mater. 186 (2020) 644–655.
[71] T. Hasegawa, T. Yakou, U.F. Kocks, Length changes and stress effects during recovery of deformed aluminum, Acta Metall. 30 (1982) 235–243.